A detailed structural characterization of quartz on heating through the α−β phase transition

M. G. Tucker[1], D. A. Keen[2,†] AND M. T. Dove[1,*]

[1] Department of Earth Sciences, University of Cambridge, Downing Street, Cambridge, CB2 3EQ, UK
[2] ISIS Faculty, Rutherford Appleton Laboratory, Chilton, Didcot, Oxfordshire OX11 0QX, UK

ABSTRACT

Total neutron scattering measurements, analysed using a modification of the reverse Monte Carlo modelling method to account for long-range crystallographic order, have been used to describe the temperature-dependent behaviour of the structure of quartz. Two key observations are reported. First, the symmetry change associated with the displacive α−β phase transition is observed in both the long-range and short-range structural correlations. Secondly, some aspects of the structure, such as the Si−O bond length and the thermally-induced dynamic disorder, the latter of which sets in significantly below the transition, are relatively insensitive to the phase transition. These results are used to show that the α-domain model of the β-phase disorder is inappropriate and that the classical soft-mode picture of the phase transition is too simplistic. Instead, it is argued that the structural behaviour is best described in terms of its ability to respond to low-frequency, high-amplitude vibrational modes. This view is supported by additional single-crystal diffuse neutron scattering measurements.

Introduction

QUARTZ, SiO_2, is a much-studied material, investigated by crystallographers, solid-state physicists and mineral scientists over many years. The crystal structures of the α (low) and β (high) phases were first deduced in the 1920s by Bragg and Gibbs (1925) and Gibbs (1925). Since their pioneering work, many studies have been carried out to refine the structural models further using both neutron and X-ray single crystal diffraction (e.g. Wright and Lehmann, 1981; Kihara, 1990). Much of this work has been reviewed in considerable detail by Heaney (1994).

Despite the wealth of documented research on quartz, it is perhaps surprising that there is still no clear, experimentally verified, picture of what

actually happens to the quartz structure on heating from α- to β-quartz through the displacive phase transition at T_c = 846 K. This can begin to be understood when it is considered that few experimental probes are able to take a 'holistic' view of the structure. Most studies tend to focus on either the long-range structural response to the phase transition (e.g. Bragg diffraction measurements), or the short-range (e.g. spectroscopic measurements), rather than attempting to rationalize both aspects of the structure simultaneously. Interpretations have thus tended to follow two extreme perspectives. First is the so-called domain model for the β-phase. It is assumed that the atoms hop between the positions corresponding to different α-domains, so that there is dynamic disorder in the high-symmetry β-phase, and on cooling the atoms progressively occupy the positions corresponding to one domain in the low- symmetry α-phase. Secondly, there is the classical soft-mode picture, in which the atoms vibrate around mean positions which change (through symmetry breaking) on cooling

* E-mail: martin@esc.cam.ac.uk
† Present address: Department of Physics, Oxford University, Clarendon Laboratory, Parks Road, Oxford, OX1 3PU, UK

through T_c and the displacive mode acts as the classical soft mode. We have shown in a previous letter (Tucker *et al.*, 2000*a*) that neither of these two models provide a completely satisfactory picture of the structure of quartz, and in fact there is an additional, perhaps dominant, contribution to the disorder in the β-phase from low-energy high-amplitude vibrations that become excited as a result of the phase transition.

This paper describes the new analysis methods used to characterize the structure of quartz in greater detail. These methods are based on reverse Monte Carlo modelling (Dove *et al.*, 2000*b*; Keen and Dove, 2000) using neutron total scattering data, the new feature being the use of extracted Bragg intensities to refine structural models (Tucker *et al.*, 2001). This approach was used to generate atomic models of the structure of quartz over a wide range of temperatures, which were interpreted to provide a complete description of the structural changes in quartz as a function of temperature. In addition, new single crystal diffuse neutron scattering results are presented which support the interpretations given here.

Experimental

Total neutron scattering

Total neutron scattering data were obtained from quartz at a number of temperatures on the LAD diffractometer (Howells and Hannon, 1999) at the ISIS spallation neutron source. The sample was a finely-ground powder of natural quartz, contained in a cylindrical thin-walled vanadium can of 8 mm diameter. This was mounted onto the 'cold finger' of a closed-cycle helium refrigerator (CCR) for measurements at 20, 150 and 290 K, and inside a standard vanadium-foil furnace for measurements at and above room temperature (at 293, 473, 673, 793, 823, 833, 843, 857, 863, 973 and 1073 K). Data were collected on three separate occasions, counting for between 3 and 4 h per temperature. Separate measurements of a similar empty can within CCR and furnace, empty CCR and furnace, standard vanadium rod, silicon sample and empty instrument were also made for subsequent instrument calibration and data correction.

The LAD instrument collected scattering data in detector banks centred on seven different scattering angles, 2θ. Data from all the detector banks were corrected and merged in a manner routinely used for the treatment of scattering data from liquid and amorphous samples (Howe *et al.*, 1989) to produce a normalized differential cross-

section, $d\sigma/d\Omega$, over the range $0.2 < Q < 40$ Å^{-1} for each temperature. Data from the back-scattering detector banks ($2\theta \approx 147°$), which have the highest Q-space resolution, were also corrected separately to produce powder patterns for Rietveld refinement.

The phase transition was carefully traversed in small temperature steps to ensure that data were taken as close to T_c as possible. T_c was actually found to be close to the nominal temperature of 858 K (~10 K above the accepted value), indicating that there was a progressive positive offset between the measured temperature in the furnace and the actual sample temperature. All data in this paper will be plotted against measured temperature, since it is unlikely that this temperature difference is linear.

Single crystal diffuse neutron scattering

Diffuse neutron scattering data from a ~30° section of the *hk*0 reciprocal lattice plane of quartz were collected at a number of temperatures using the PRISMA spectrometer (Harris and Bull, 1998) at ISIS. A 30 mm long natural quartz crystal with hexagonal cross-section and 11 mm mean diameter was mounted, using tantalum wire, with the rod axis vertical inside a standard vanadium foil neutron furnace. This was aligned on PRISMA with the *c*-axis vertical and data were collected as a function of neutron time-of-flight using sixteen diffraction detectors in the equatorial plane centred on $2\theta = 90°$, with each detector separated by $2\theta = 1°$ from its immediate neighbour. Data were collected using five different crystal settings per temperature and measuring for around 30 min per setting. The initial measurement was at room temperature, followed by 1073, 973, 923, 873, 853, 833, 773, 673 and 573 K. Data were normalized to a vanadium standard and rebinned onto the *hk*0 reciprocal lattice plane for quartz using standard PRISMA routines (Harris and Bull, 1998).

Data analysis

Rietveld refinement

Time-of-flight Rietveld refinements of the back-scattering diffraction data used the program TF12LS (David *et al.*, 1992) which is based on the Cambridge crystallographic subroutine library (Brown and Matthewman, 1992). The quality of the fit to the experimental diffraction data was assessed using the normal χ^2 statistic defined as

$\chi^2 = R_{wp}^2/R_{exp}^2$, where the weighted profile R-factor, R_{wp}, is given by

$$R_{wp}^2 = \sum_{N_d} \frac{(I_{obs} - I_{calc})^2}{(\sigma I_{obs})^2} / \sum_{N_d} \frac{(I_{obs})^2}{(\sigma I_{obs})^2} \quad (1)$$

The summations are over the N_d data points used in the fit. The expected R-factor is then given by

$$R_{exp}^2 = (N_d - N_p) / \sum_{N_d} \frac{(I_{obs})^2}{(\sigma I_{obs})^2} \quad (2)$$

where N_p is the number of fitted parameters. I_{obs} and I_{calc} are the observed and calculated intensities respectively and σI_{oba} is the estimated standard deviation on I_{obs} derived from the counting statistics. In addition, Bragg intensities were extracted using the Pawley method (Pawley, 1981) within the same routines (David *et al.*, 1992). These were used in the reverse Monte Carlo modelling described below.

Total scattering correlation functions

The total scattering structure factor, $F(Q)$, may be determined from the differential cross-section (Keen, 2001)

$$\frac{1}{N}\frac{d\sigma}{d\Omega} = F(Q) + \sum_{i=1}^{n} c_i \overline{b_i^2} \quad (3)$$

where $4\pi \sum_{i=1}^{n} c_i \overline{b_i^2}$ is the total scattering cross-section of the material and the summation is over the n atom types. There are N atoms in the material and c_i is the proportion of atom type i. $F(Q)$ is related to the total radial distribution function, $G(r)$, by the Fourier transform

$$G(r) = \frac{1}{(2\pi)^3 \rho_0} \int_0^\infty 4\pi Q^2 F(Q) \frac{\sin Qr}{Qr} dQ \quad (4)$$

with average atom number density $\rho_0 = N/V$ (in atoms/Å^3).
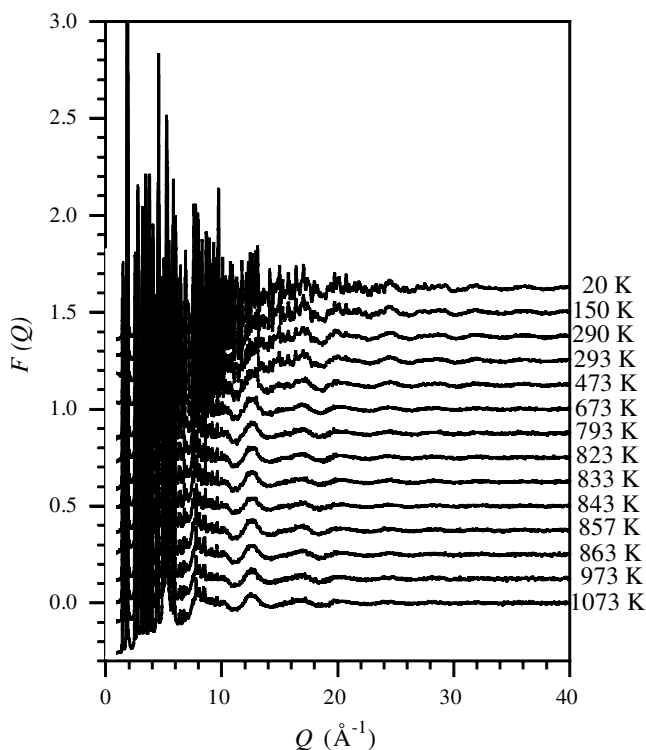
FIG. 1. Neutron total scattering structure factors of quartz over a wide range of temperatures. Each successive structure factor has been offset vertically by +0.125 for clarity.
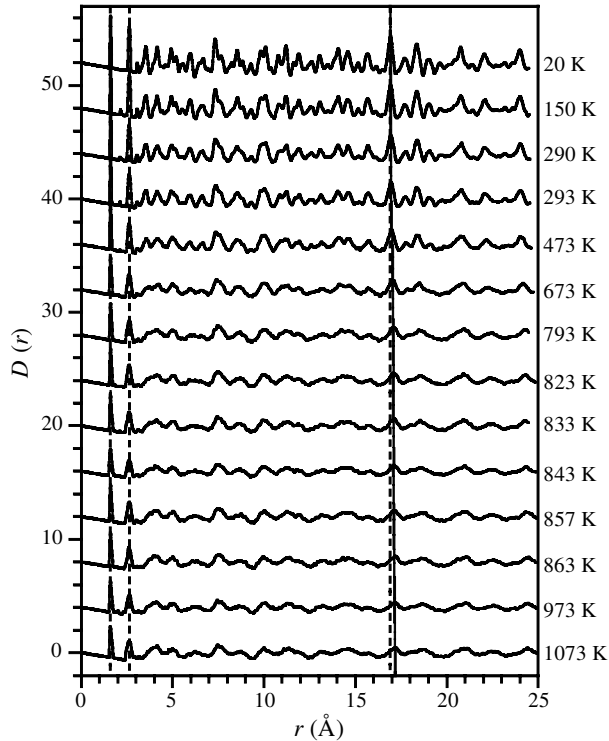
FIG. 2. Neutron weighted total pair correlation functions $D(r)$ over a wide range of temperatures. Each successive function has been offset vertically by +4.0 for clarity. The two vertical dashed lines at low-r indicate the positions of the Si—O and O—O distances whereas the full line at $r \approx 17$ Å reflects the macroscopic expansion of quartz (see text for details).

$G(r)$ may also be defined in terms of the partial radial distribution functions $g_{ij}(r)$,

$$G(r) = \sum_{i,j=1}^{n} c_i c_j \overline{b}_i \overline{b}_j \left(g_{ij}(r) - 1 \right) \qquad (5)$$

where

$$g_{ij}(r) = \frac{n_{ij}(r)}{4\pi r^2 \rho_j \mathrm{d}r} \qquad (6)$$

$n_{ij}(r)$ are the number of particles of type j between distances r and $r + \mathrm{d}r$ from a particle of type i and $\rho_j = c_j \rho_0$. Two other commonly used correlation functions, $D(r)$, the differential correlation function and $T(r)$, the total correlation function are then defined as

$$D(r) = 4\pi r \rho_0 G(r) \qquad (7)$$

and

$$T(r) = 4\pi r \rho_0 \left\{ G(r) + \left(\sum_{i=1}^{n} c_i \overline{b}_i \right)^2 \right\} \qquad (8)$$

The normalized total scattering structure factors, $F(Q)$, are shown in Fig. 1. The significant structure in $F(Q)$ at $Q_{\max} \approx 40$ Å^{-1} will lead to problems of truncation within the Fourier transform in equation 4 at $Q_{\max}$. In order to circumvent this, the inverse method MCGR (Pusztai and McGreevy, 1997) was used to determine $G(r)$. Here a model total radial distribution function, $G_{\mathrm{model}}(r)$, is constructed between 0 and $r_{\max}$. $G_{\mathrm{model}}(r)$ is iteratively varied and Fourier transformed to $F_{\mathrm{model}}(Q)$ using the inverse relation

$$F(Q) = \rho_0 \int_0^{\infty} 4\pi r^2 G(r) \frac{\sin Qr}{Qr} \mathrm{d}r \qquad (9)$$
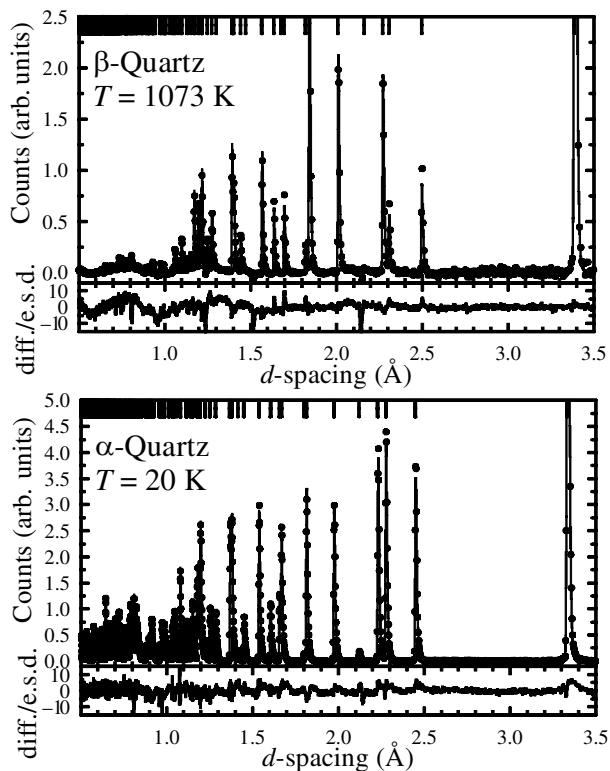
FIG. 3. Least squares refinement of neutron diffraction data from α-quartz at 20 K (lower plot) and from β-quartz at 1073 K (upper plot). The dots are the experimental data from the back-scattering detector banks on the LAD diffractometer and the full lines are the profiles calculated using the refined structural models described in the text. The tick marks at the top of both main panels show the calculated positions of the Bragg peaks and the smaller panels show the differences (measured-calculated) divided by the estimated standard deviation of the data points.

for comparison with the with experimental $F_{\mathrm{expt}}(Q)$. The difference between $F_{\mathrm{model}}(Q)$ and $F_{\mathrm{expt}}(Q)$ is used to determine which iterations are accepted. When this difference is within a predefined limit, $G_{\mathrm{model}}(r)$ is a good representation of $G_{\mathrm{exp}}(r)$ for $0 < r < r_{\mathrm{max}}$. The process can then be repeated any number of times until the desired statistical accuracy is obtained for the average $G_{\mathrm{model}}(r)$. This method bypasses the truncation errors inherent in the Fourier transform $F(Q) \rightarrow G(r)$ and, provided that $r_{\mathrm{max}} > 2\pi/\Delta Q$ (where ΔQ is the width of the narrowest Bragg peak), does not introduce different truncation errors on the inverse Fourier transform. The $D(r)$ produced using MCGR are shown in Fig. 2. The pair correlation functions are then fitted in the reverse Monte Carlo modelling described below.

Finally, if $G(r)$ is calculated from a configuration of atoms of finite size, using equations 5 and 6, then the $F(Q)$ from this $G(r)$ (via equation 9) will contain truncation errors. Hence, in order to make a valid comparison between the $F_{\mathrm{calc}}(Q)$ from, for example, an RMC configuration, $F_{\mathrm{expt}}(Q)$ must first be convoluted with the Fourier transform of a box function of size $L/2$, where L is the shortest side of the (orthorhombic) configuration box.

$$F_{\mathrm{expt}}^{\mathrm{box}}(Q) = \frac{1}{\pi} \int_{-\infty}^{\infty} (Q') \frac{\sin(L/2(Q - Q'))}{Q - Q'} \mathrm{d}Q' \quad (10)$$

where $F_{\mathrm{expt}}^{\infty}(Q)$ is approximated by an $F_{\mathrm{expt}}(Q)$ with suitably sharp Q-space resolution. $F_{\mathrm{expt}}^{\infty}(Q)$ has lower and broader Bragg peaks and represents

a finite range in real space. This function was also fitted in the reverse Monte Carlo modelling.

Reverse Monte Carlo modelling

The reverse Monte Carlo modelling method has been described in detail elsewhere (McGreevy and Pusztai, 1988; McGreevy, 1995). In essence, scattering functions are calculated from a three-dimensional arrangement of atoms each time an atom is moved and compared with the equivalent experimentally determined functions. Atoms are selected at random and moved a random amount up to a pre-defined limit. Atom moves are accepted on the basis of χ^2_{RMC} defined as (for example),

$$\chi^2_{RMC} = \sum_{k=1}^{K} \sum_i \left[F_{calc}(Q_i)_k - F_{exp}(Q_i)_k\right]^2 / \sigma_k(Q_i)^2$$
$$+ \sum_{l=1}^{L} \sum_i \left[G_{calc}(r_i)_l - G_{exp}(r_i)_l\right]^2 / \sigma_l(r_i)^2$$
$$+ \sum_{j=1}^{J} \left(f_j^{req} - f_j^{RMC}\right)^2 / \sigma_j^2 \qquad (11)$$

to include comparison with K structure factors, L radial distribution functions and J constraints. $\sigma_k(Q_i)$ and $\sigma_l(r_i)$ are related to the experimental error but are usually (for neutron diffraction) treated as independent of Q_i and r_i respectively. If χ^2_{RMC} is reduced as a result of the atom move, then the move is accepted and if χ^2_{RMC} increases it is accepted with a probability $\exp(-\Delta\chi^2_{RMC}$, where $\Delta\chi^2_{RMC} = \chi^2_{new} - \chi^2_{old}$. Atoms are moved until there is little further reduction in χ^2_{RMC} and convergence is achieved.

The third term in equation 11 is included when constraints are used to limit possible atom moves. f_j^{req} and f_j^{RMC} are the required value of constraint, j, and the value calculated from the RMC generated configuration, respectively. σ_j can be used as a weighting term to influence the strength of any particular constraint. These constraints are extremely important for network systems, where topology must be retained. Here, the constraints have the form (Keen, 1997, 1998)

$$\sum_{\substack{Si-O \\ bonds}} (r_{Si-O} - R_{Si-O})^2 / \sigma_{Si-O}^2 +$$
$$\sum_{\substack{O-Si-O \\ angles}} (\theta_{O-Si-O} - \Theta_{O-Si-O})^2 / \sigma_{O-Si-O}^2 \quad (12)$$

where R_{Si-O} is the position of the lowest-r peak in $T(r)$ and Θ_{O-Si-O} is the ideal tetrahedral angle. The first summation constrains Si—O bonds such that the position and width of the lowest-r peak in $T(r)$ is reproduced, and the second maintains regular SiO$_4$ tetrahedra. The combined effect of both of these two constraints is to force the model to retain a continuous network of corner-sharing SiO$_4$ tetrahedra.

Finally, the Bragg intensities are calculated from the model, using the following equation

$$I(\mathbf{Q}) = \frac{1}{2\pi r N} \left| \sum_j \overline{b_j} \exp(i\mathbf{Q} \cdot \mathbf{r}_j) \right|^2 \qquad (13)$$

evaluated at reciprocal lattice vectors, $\mathbf{Q} = \mathbf{H}$. Here the summation is over the N atoms in the model and $\mathbf{r}_j$ is the vector joining atom j to an arbitrary origin (it is assumed that the model is a supercell of the unit cell). These are compared to the experimental data extracted using the Pawley method (Pawley, 1981) and used as an additional constraint to the model

$$\sum_{\mathbf{H}} (sI_{exp}(\mathbf{H} - I_{calc}(\mathbf{H}))^2 / \sigma_{\mathbf{H}}^2 \qquad (14)$$

where s is a scale factor and $I(\mathbf{H})$ is the intensity of the $hk1$ Bragg reflection. This constraint introduces an element of $\mathbf{Q}$-dependence into the model, reduces the disorder in the final model and improves the consistency between the average structure and the averages obtained from RMC configurations (Tucker *et al.*, 2001).

Hence, for each temperature, an RMC model of quartz was refined by fitting to one total structure factor, one total radial distribution function, a set of extracted Bragg intensities whilst constrained by an Si—O bond length and O—Si—O tetrahedral angle. The starting models consisted of a $10 \times 10 \times 10$ supercell of an orthorhombic unit cell of quartz (containing 18 atoms) using the average atom positions determined from Rietveld refinement of the diffraction data at each temperature. Typical minimizations took 80 h using a Silicon Graphics R5000 processor.

Results

In general, the average structures of the two phases of quartz are complicated by twinning and the sense of the SiO$_4$ tetrahedral network topology. The high-temperature hexagonal β-phase structure
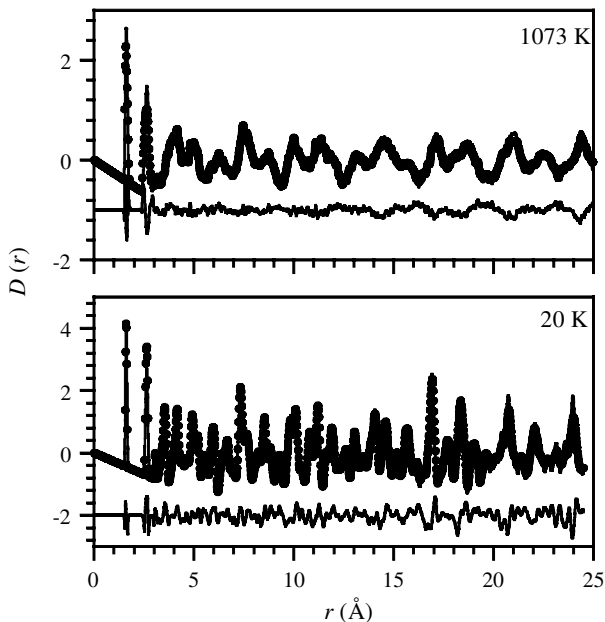
FIG. 4. RMC refinement of neutron diffraction data from α-quartz at 20 K (lower plot) and from β-quartz at 1073 K (upper plot). The dots are the experimental $D(r)$ data obtained using MCGR on $F(Q)$ and the full lines are $D(r)$ calculated from the refined RMC structural models described in the text. The lower trace in each plot shows the difference (measured-calculated), offset vertically by −1 (1073 K) and −2 (20 K).

consists of either right-handed (space group $P6_222$) or left-handed (space group $P6_422$) helices parallel to the c-axis (Heaney, 1994). On cooling into the α-phase, the average positions of the SiO$_4$ tetrahedra are seen to rotate about $\langle 100 \rangle$ directions by an amount δ to give rise to a trigonal structure in space groups $P3_221$ and $P3_121$ for right- and left-handed quartz respectively. The handedness is preserved through T_c and the two enantiomorphs are known as the Brazil twins of quartz. In addition, the rotation, δ, may occur in either a positive or negative sense within either left- or right-handed quartz to produce Daupiné twins. A further complication concerns the appearance of an incommensurate phase over a very small (~1 K) temperature range between the α and β phases (reviewed by Heaney and Veblen, 1991). This phase is very difficult to stabilize effectively, and our measurements, even those close to T_c, do not see the incommensurate phase.

Rietveld refinements were performed in space group $P3_121$ and $P6_422$ for α- and β-quartz respectively. The standard settings of the *International Tables for Crystallography* (Hahn, 1996) were used throughout, namely Si was located at $3a$ $(x,0,1/3)$ and O at $6c$ (x,y,z) for α-quartz, whereas for β-quartz, Si was placed at $3c$ $(1/2,0,0)$ and O on $6j$ $(x,2x,1/2)$ in their respective space groups. The two structures may be compared by noting that the β-phase, with a $+c/3$ change in origin places Si atoms at $(1/2,0,1/3)$ and
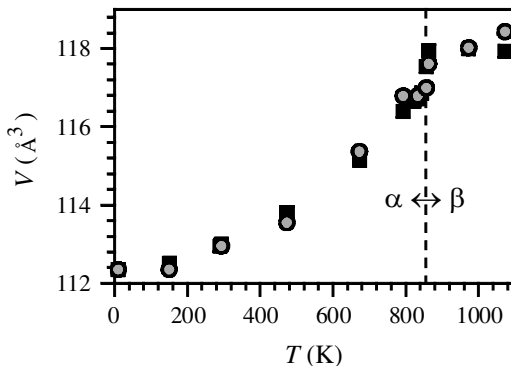
FIG. 5. Comparison of the temperature dependence of the unit-cell volume of the average structure of quartz (squares) with the cube of the position of a peak in $D(r)$ at high-r (circles), scaled to coincide at 20 K.
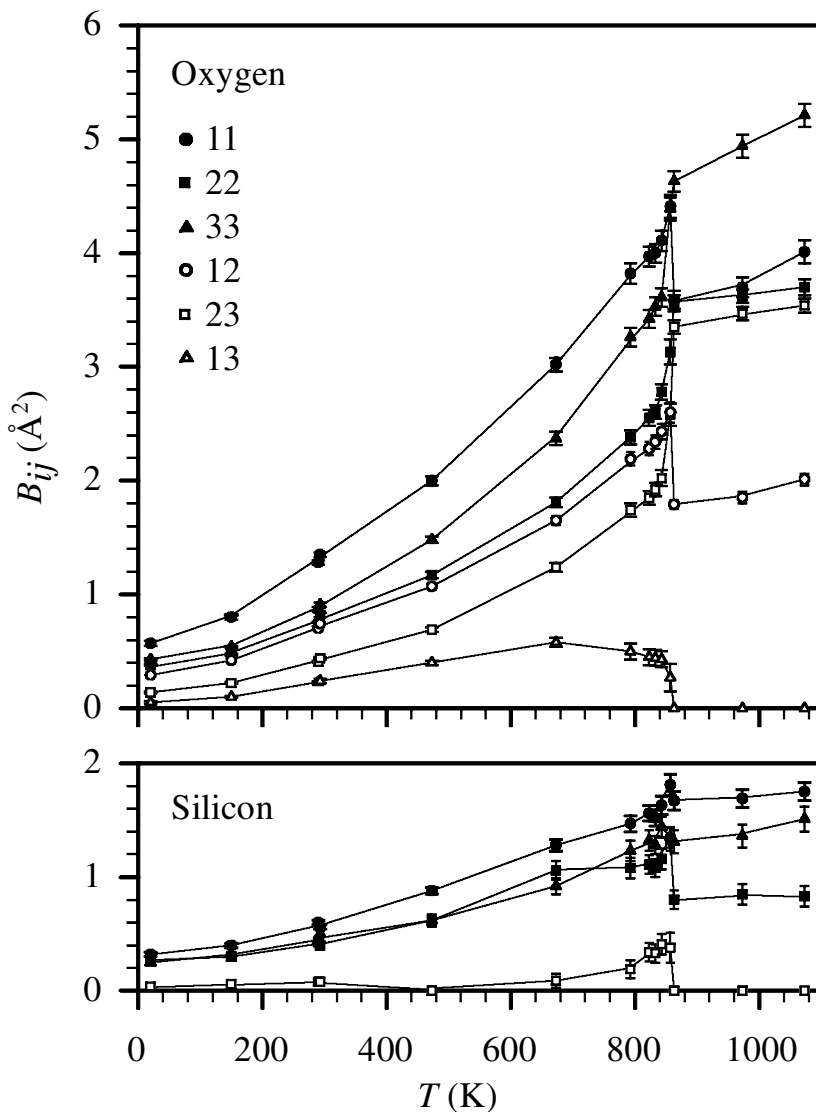
FIG. 6. Temperature dependence of anisotropic atomic displacement parameters in quartz.

O atoms at $(2x,x,1/6)$. The data quality, both in terms of statistical accuracy and short *d*-spacing reflections made refinements of fully anisotropic atomic displacement parameters possible for all temperatures. Figure 3 shows fits to the neutron powder patterns from quartz at the lowest and highest temperatures measured; Table 1 summarizes the results from these temperatures, showing that good fits were obtained and yielding precise structural parameters.

The fits to $D(r)$ from RMC refinements of quartz at 20 and 1073 K are shown in Fig. 4. Good agreement was obtained at all temperatures to $D(r)$, $F(Q)$ and the $I(\mathbf{H})$ simultaneously and whilst maintaining the tetrahedral constraints and network topology. The two main discrepancies in Fig. 4 occur in the widths of the first two low-*r* peaks, suggesting that the constraints produced distributions of Si—O and O—O nearest-neighbour distances that were slightly too sharp, and at

TABLE 1. Summary of results from Rietveld refinements of neutron diffraction data from quartz at 20 and 107 K. V/Z is the unit-cell volume per SiO_2 formula unit and (F) denotes a parameter which is fixed by symmetry.

		α-quartz	β-quartz
T (K)		20	1073
Space group		$P3_121$	$P6_422$
Lattice parameters	a(Å)	4.9019(1)	4.9965(1)
	c(Å)	5.3988(1)	5.4543(1)
	V/Z (Å^3)	37.45	39.31
Atom positions	Si (x)	0.4673(2)	1/2 (F)
	(y)	0 (F)	0 (F)
	(z)	1/3 (F)	0 (F)
	O (x)	0.4130(1)	0.4169(4)
	(y)	0.2711(1)	$x/2$
	(z)	0.21720(8)	5/6 (F)
Thermal Parameters	Si B11 (Å^2)	0.32(2)	1.75(8)
	B22 (Å^2)	0.27(2)	0.83(9)
	B33 (Å^2)	0.25(2)	1.51(11)
	B12 (Å^2)	B22/2	B22/2
	B13 (Å^2)	B23/3	0 (F)
	B23 (Å^2)	0.04(2)	0 (F)
	O B11 (Å^2)	0.57(2)	4.01(10)
	B22 (Å^2)	0.38(1)	3.70(7)
	B33 (Å^2)	0.43(1)	5.21(10)
	B12 (Å^2)	0.29(1)	B11/2
	B13 (Å^2)	0.05(1)	0 (F)
	B23 (Å^2)	0.139(9)	3.54(6)
Goodness-of-fit	χ^2	10.73	9.58
Weighted R-factor	R_w	3.46	2.99
Expected R-factor	R_{exp}	1.06	0.97
Number of data points	N_d	2946	2947
Number of Bragg peaks	N_B	3658	1926
Number of fitted parameters	N_p	31	24

large-r, where again the RMC model produced sharper peaks than observed in the data. This latter effect is due to the finite Q-space resolution in $F(Q)$, which causes the peaks in $D(r)$ to broaden, with an additional contribution to the peak width which is proportional to r^2 (Toby and Egami, 1992).

A cursory inspection of Figs 1 and 2 suggests that the onset of disorder within quartz is gradual and without a clearly defined phase transition. In addition, the disorder sets in at temperatures significantly below T_c. The Bragg peaks reduce in intensity steadily with increased temperature over the whole temperature range as the peaks in $D(r)$ become broader. There is little difference in $F(Q)$ or $D(r)$ data just above and below T_c (compare plots at 857 and 863 K). However, the phase transition can be seen in the details of the data. Figure 5 compares the volume expansion of quartz, determined from Rietveld refinement with the position of the peak in $D(r)$ at ~17 Å shown as a full line in Fig. 2. The unit-cell volume shows the same behaviour around the phase transition as seen by other workers (Carpenter et al., 1998) and this is mimicked, albeit less precisely due to peak broadening with increased temperature, by the position of a high-r peak in $D(r)$.

The anisotropic atomic displacement parameters also show this combination of large thermal disorder, beginning at relatively low temperatures and changes at the phase transition (see Fig. 6). The oxygen atomic displacement parameters show large anisotropy at all tempera-
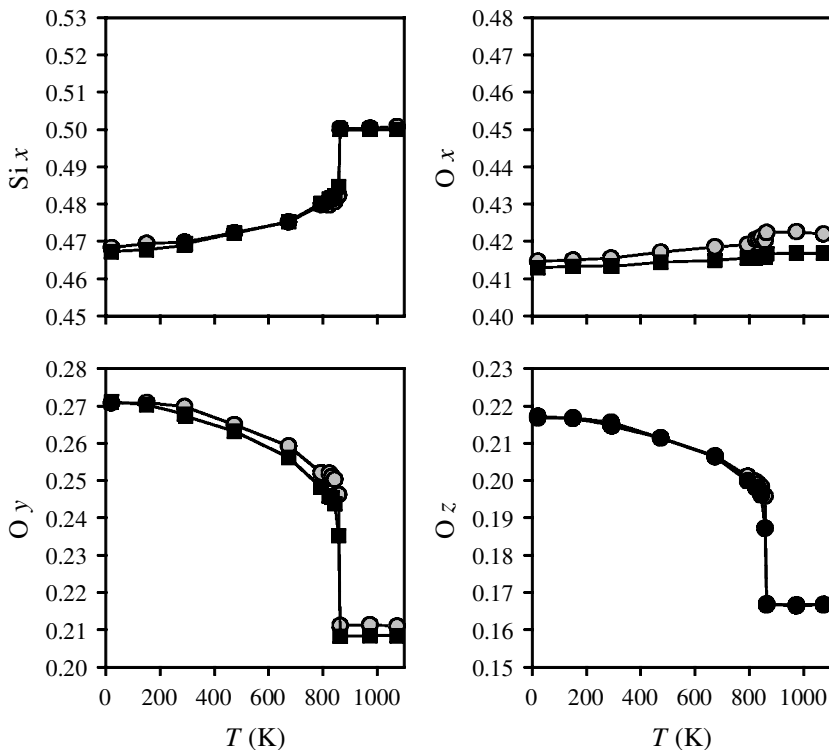
FIG. 7. Temperature dependence of structural parameters in quartz taking into account the $c/3$ origin shift in β-quartz with respect to the standard settings. The squares are from Rietveld refinements and the circles are average values taken from RMC configurations (see text for details).

tures, becoming more pronounced as temperature increases whereas the silicon distribution implied by the atomic displacement parameters is more symmetric. This is indicative of librational motion of 'rigid' SiO_4 tetrahedral units. At T_c, the symmetry change introduces changes to the atomic displacement parameters, with some becoming zero, but the magnitude of the overall disorder does not change significantly.

Figure 7 shows the development with temperature of the silica and oxygen atom coordinates, showing both the Rietveld refined values and those obtained from the RMC refined configurations. The latter were obtained by superposing all the atoms within the configuration onto one unit cell and determining a mean position from the resulting atom density distribution. These parameters, together with the unit-cell parameters, may be used to calculate δ, the tetrahedral tilt angle which has been taken as the order parameter of the α–β phase transition (Grimm and Dorner,
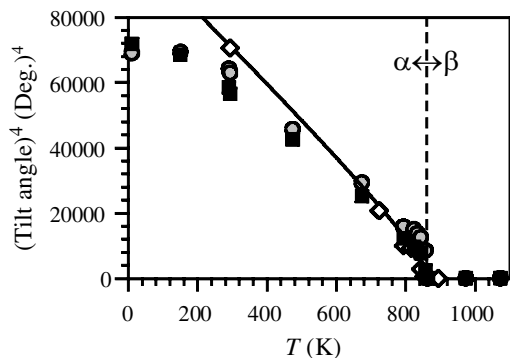
FIG. 8. Temperature dependence of the fourth power of the average SiO_4 tetrahedral tilt angle, δ. Filled squares and circles represent data from Rietveld and RMC refinements respectively and the open diamonds and straight line represent experimental XRD data (Young, 1962; Jay, 1933) and results of a Landau free energy function (Grimm and Dorner, 1975) respectively.

1975). This is shown in Fig. 8, together with previous X-ray diffraction results (Young, 1962; Jay, 1933) and a fit to the X-ray data using the following equation (Grimm and Dorner, 1975):

$$\delta = \frac{2}{3}\delta_0^2 \left(1 + \sqrt{1 - \frac{3}{4}\frac{T - T_0}{T_c - T_0}} \right) \qquad (15)$$

where δ_0 is the jump in tilt angle at T_c (7.3°), and T_0 is the temperature at which the phase transition would occur if it were second order. ($T_0 = T_c - 10$ K).

The average structure of quartz is shown for three temperatures in Fig. 9. The development of structural disorder as temperature is raised while still in the α-phase is seen in the sizes of the thermal ellipses; the change in symmetry on passing through T_c is evident when the central channel in this projection becomes a regular hexagon in the β-phase. Figure 10 shows a (100) layer of a RMC configuration, together with the average structure produced from the configuration, at three similar temperatures to those in the structure plots in Fig. 9. Whereas the 20 K configuration shows a well-ordered structure, both high temperature configurations are highly disordered. The disorder appears random in so far as there are no clear domains within the configurations, although the underlying trigonal or hexagonal symmetry is preserved, as seen in the average structures obtained from the configurations.

So far we have demonstrated remarkable consistency in the average structures obtained via Rietveld refinement of the Bragg peaks in the powder patterns and the average structural parameters obtained from the RMC refinements. In addition however, the RMC models (as shown in Fig. 10) may also be used to determine other instantaneous correlations such as local bond lengths and angles. Figure 11 shows that the Rietveld refined model accommodates the increasing disorder in the structure by reducing the size of the SiO_4 tetrahedra. This is unlikely to be physical (Liebau, 1985). In contrast, the instantaneous correlation functions obtained from the RMC models show increasing Si−O (and O−O) nearest-neighbour interatomic distances with increasing temperature and are in line with what might be expected (Tucker *et al.*, 2000b). We also note that the 'unphysical' behaviour may also be recovered from the average structural parameters obtained from RMC configurations. The disparity between
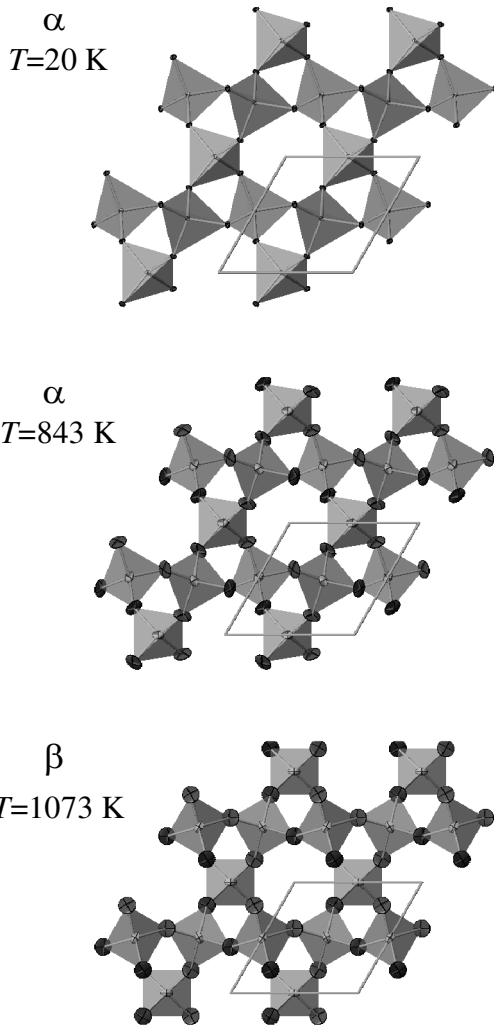
FIG. 9. The average structure of quartz obtained from least squares refinement of neutron diffraction data from α-quartz at 20 and 843 K and from β-quartz at 1073 K. The structures are plotted looking down the *c*-axis and show the SiO_4 tetrahedra and the anisotropic atomic displacement parameters of the Si and O atoms.

instantaneous and average structural parameters is clearly seen in the temperature dependence of the Si−O or O−O distances (Fig. 11). Here the instantaneous bond length (whether from the experimental or RMC derived $T(r)$) increases linearly with increasing temperature and is
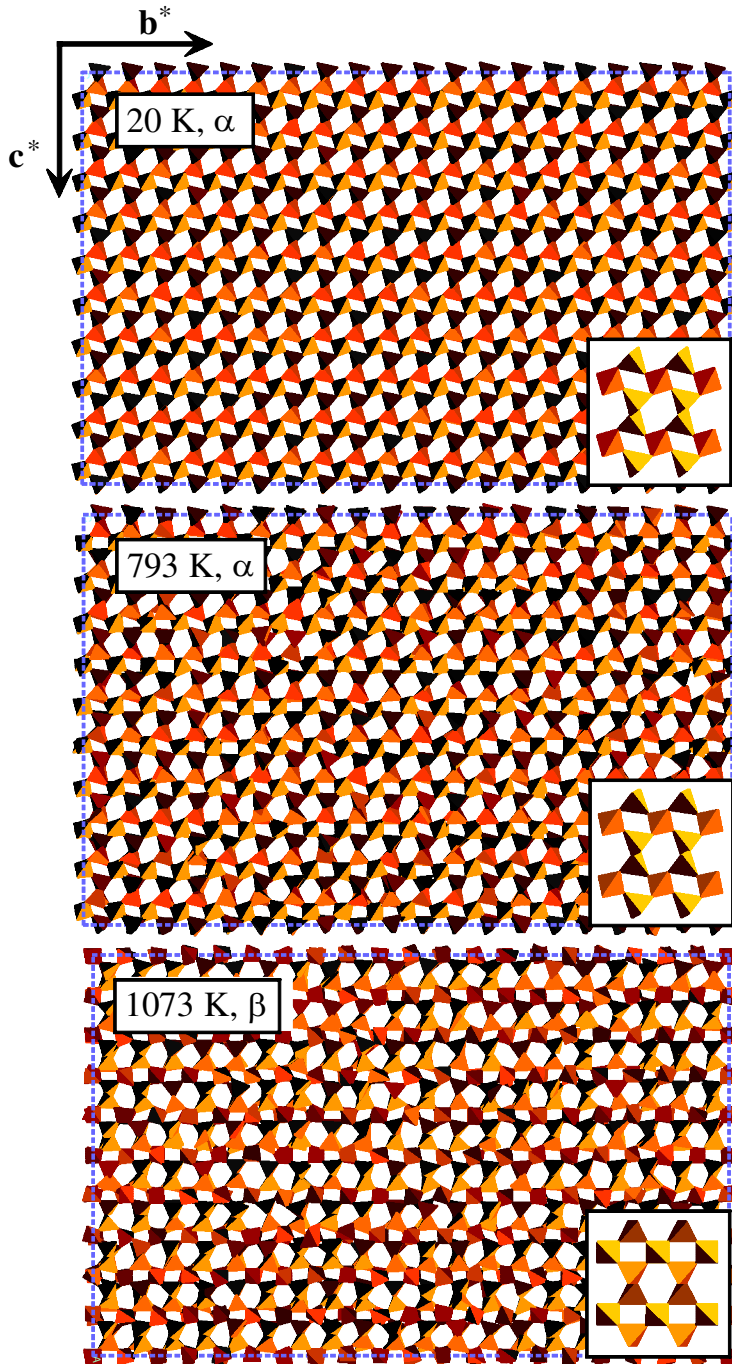
FIG. 10. (100) layers of instantaneous RMC atomic configurations of quartz represented by SiO$_4$ tetrahedra for one temperature above T_c and two below. The insets show the average structures obtained from the same configurations. In this projection the small parallelopiped spaces between tetrahedra become orthogonal in the β-phase, giving a clear representation of the symmetry change at T_c.
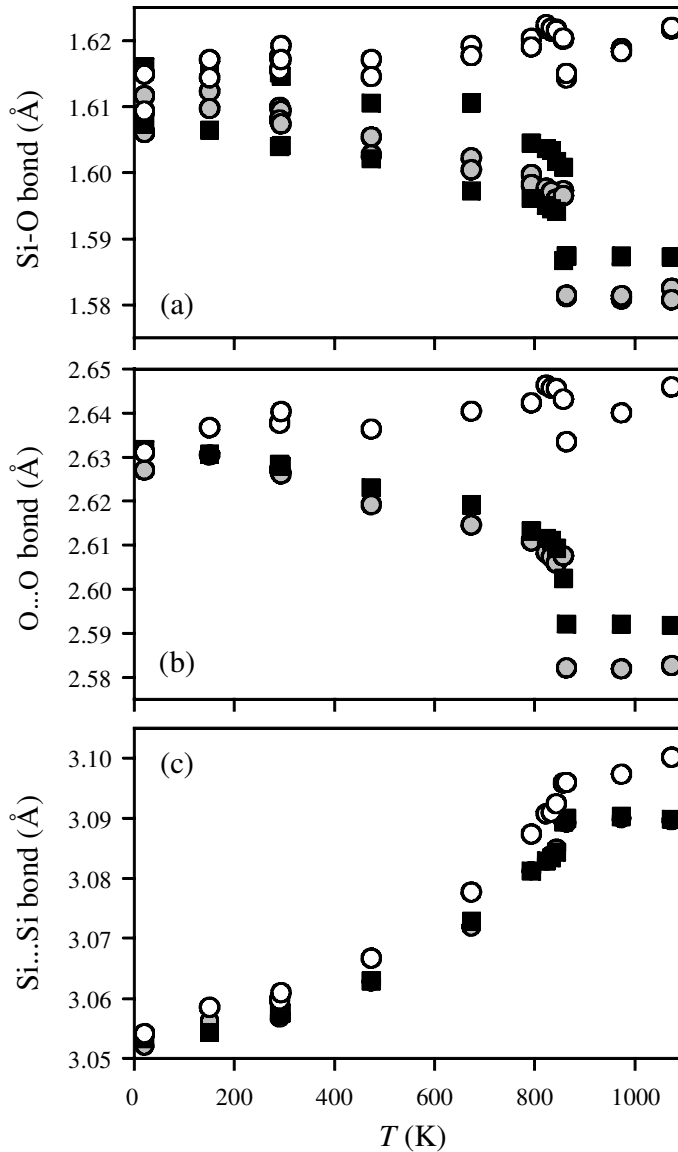
FIG. 11. Temperature dependence of the (*a*) Si−O, (*b*) O−O and (*c*) Si−Si nearest-neighbour distances in quartz. Here the filled squares and circles represent the distance between average atom positions, e.g. $\langle Si \rangle - \langle O \rangle$, given by Rietveld and RMC refinement respectively and the open circles represent the average values of the instantaneous distance, e.g. $\langle Si - O \rangle$, from the RMC models. Note that plot (*a*) shows Si−O bond lengths corresponding to those which lie approximately along the directions corresponding to the short and long bonds seen in the average structure.

independent of T_c, whereas the average bond length decreases with increasing temperature and shows a discontinuity at T_c. In Fig. 11 the Si−O instantaneous bond length has been further separated into those in the directions which are

expected to show a short and long bond. This has been achieved by taking the average of the actual bond lengths directly from the RMC configurations and not via $T(r)$. This clearly shows that the RMC configurations do indeed give new impor-
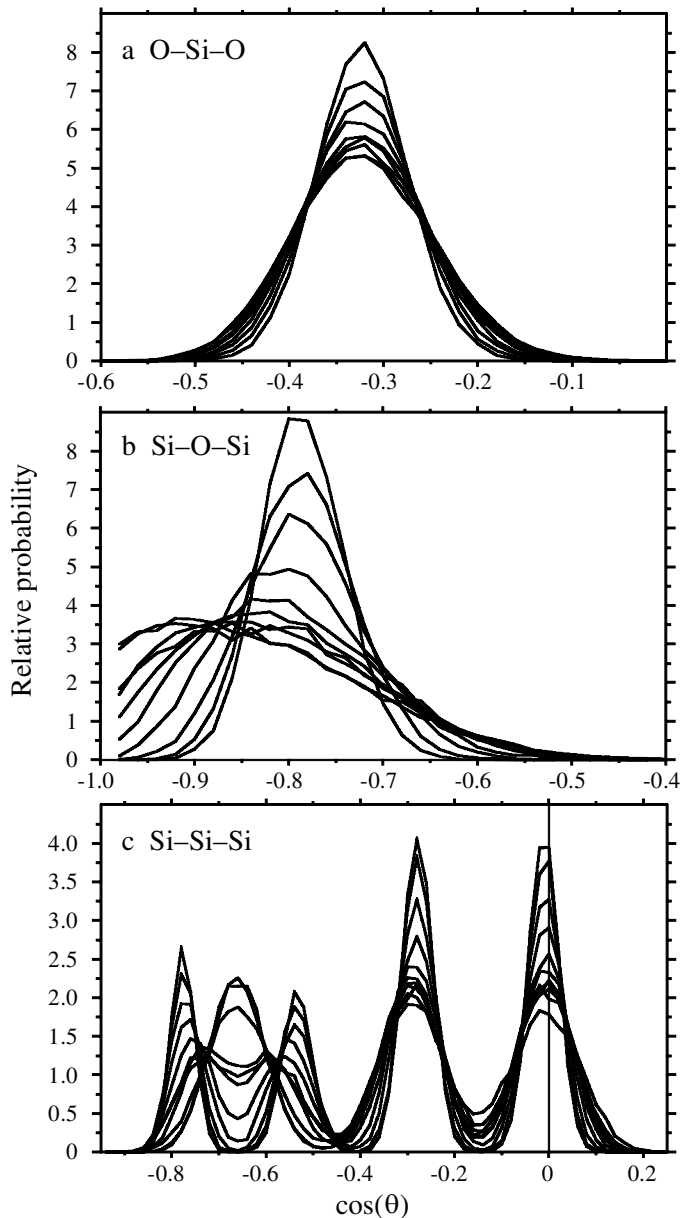
Fig. 12. The nearest neighbour atom–atom–atom angle distributions in quartz at a number of different temperatures. (*a*) O−Si−O, (*b*) Si−O−Si and (*c*) Si−Si−Si. The broader, lower peaks correspond to data at higher temperatures.

tant insight into the structural behaviour around T_c.

Taking this characterization further, Fig. 12 shows the distribution of O−Si−O, Si−O−Si and Si−Si−Si nearest neighbour angles within the

RMC configurations at a number of different temperatures. In particular, the Si−Si−Si angle distribution is seen to go from four distinct peaks within the α-phase to three in the β-phase. This is also clearly seen in Fig. 13 which plots the
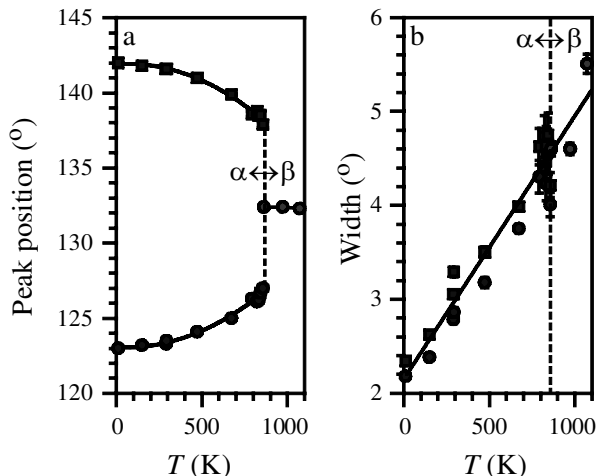
FIG. 13. The temperature dependence of (*a*) the positions and (*b*) the widths of the two peaks in the nearest neighbour Si−Si−Si angle distribution in α-quartz which form into a single peak in β-quartz (see Fig. 12).

temperature dependence of the positions and widths of the peaks in the Si−Si−Si angle distribution which coalesce in the β-phase. Whereas the positions change discontinuously at T_c, the widths increase smoothly with increasing temperature and independently of T_c. The former shows that the symmetry change at T_c is even observed in short-range correlations (the Si−Si distance is ~3 Å) and the latter indicates that the thermal disorder develops monotonically with increasing temperature and does not appear to 'notice' T_c.

Discussion

One of the key issues to understand is the inter-relationship between the phase transition and the structural disorder. As we stated previously (Tucker *et al.*, 2000*a*), there is clearly more thermally induced dynamic disorder than in either the classical soft-mode or domain models of the phase transition in quartz, and the disorder sets in at temperatures significantly below T_c. Instead of using these models, we may consider how the structure will respond to the Rigid Unit Modes (RUMs) present in quartz (Bethke *et al.*, 1987; Hammonds *et al.*, 1996). These are phonon modes that propagate without significantly distorting the SiO$_4$ tetrahedra – the tetrahedra move as rigid bodies via rotations of the Si−O−Si linkages. Since this requires significantly less energy than distorting the SiO$_4$ units, RUMs are vibrations

with the lowest frequencies and largest amplitudes (Dove *et al.*, 2000*a*; Harris *et al.*, 2000). Hence the large-amplitude rotations and transla-tions seen in the RMC configurations (Fig. 10) at higher temperatures are primarily due to the excitation of RUMs in quartz.

Detailed calculations of the RUMs in quartz (Bethke *et al.*, 1987; Hammonds *et al.*, 1996) show that although there are RUMs in both the α and β-phases, there are more RUMs in the β-phase. The frequency of these additional β-phase RUMs will increase rapidly on cooling below T_c; the soft-mode for the displacive phase transition is a RUM in the β-phase. Hence the increasing disorder in the α-phase on heating is due to the increasing amplitude (decreasing frequency) of phonon modes which become RUMs in the β-phase and the extensive disorder in the β-phase is due to the excitation of the soft mode and all the other RUMs.

In order to corroborate this description of the high-temperature behaviour of quartz, we compare the diffuse scattering in the (*hk*0) reciprocal lattice plane calculated from the RMC configurations (using equation 13 at reciprocal lattice vectors of the configuration supercell) with that measured experimentally (Fig. 14). The single crystal data at 1073 K show two strong diffuse features. The first forms a hexagon of scattering with apices at 400, 040, etc. and the second would form another complete hexagon through 800, 080, etc. except that it diverts

300 K experiment

300 K RMC

1073 K experiment

1073 K RMC
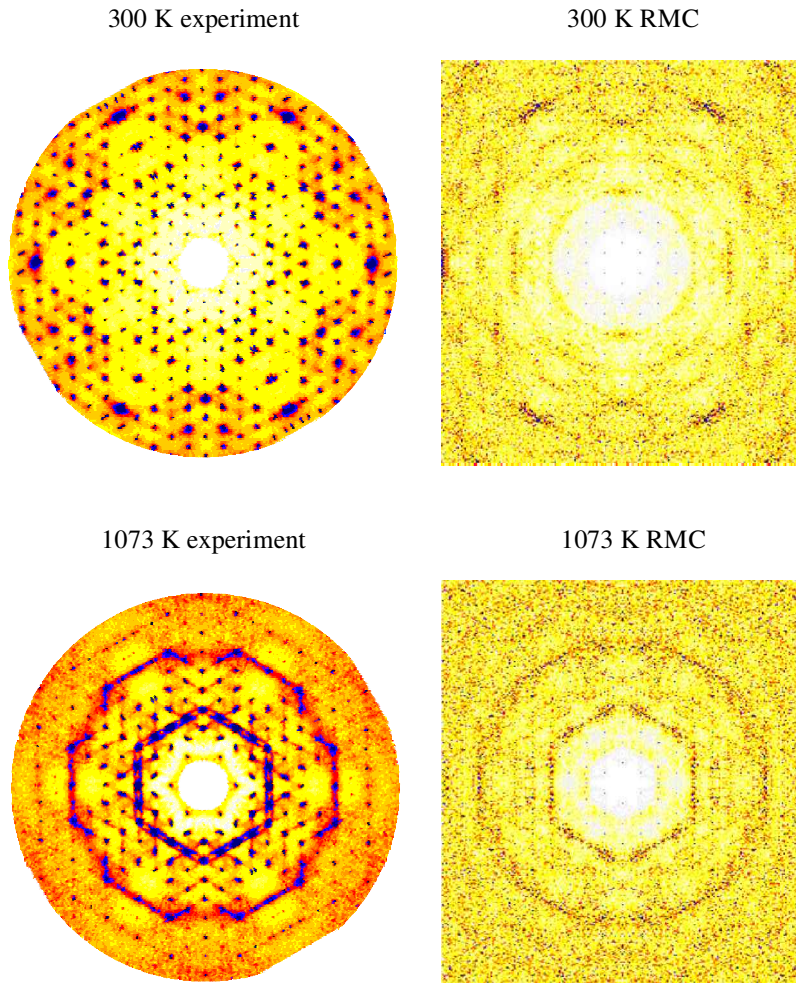
Fɪɢ. 14. The (*hk*0) reciprocal lattice of quartz at room temperature (upper panels) and at 1073 K (lower panels). The left-hand panels show experimental data collected from a single crystal of quartz measured on the PRISMA spectrometer at ISIS and the right-hand panels show the diffuse scattering calculated from the RMC configurations described in the text. The left-hand panels have been plotted using the same scale, as have the two right-hand panels.

towards 600, 060, etc. at the corners. The strongest 400 hexagon of diffuse scattering is consistent with much earlier X-ray photographs from quartz (Arnold, 1965). All the strong diffuse streaks are in (ζ00) directions and pass through Bragg peaks. Calculations predict the existence of three lines of RUMs in this plane (Hammonds *et al.*, 1996) and of these, the Σ (ζ 00) mode is the only one which only exists as a RUM in the β-phase. This explains why this diffuse scattering

is not observed in the room temperature single crystal data (Fig. 14). The other lines of RUMs which should be present in both phases (i.e. the λ (ζζ0) and *T* (1/2−ζ,2ζ,0) modes) are not observed at any temperature. This suggests that, of these three modes, the Σ (ζ00) mode has the strongest neutron or X-ray weighted structure factor in β-quartz.

The diffuse scattering calculated from the RMC models show the same features as the single
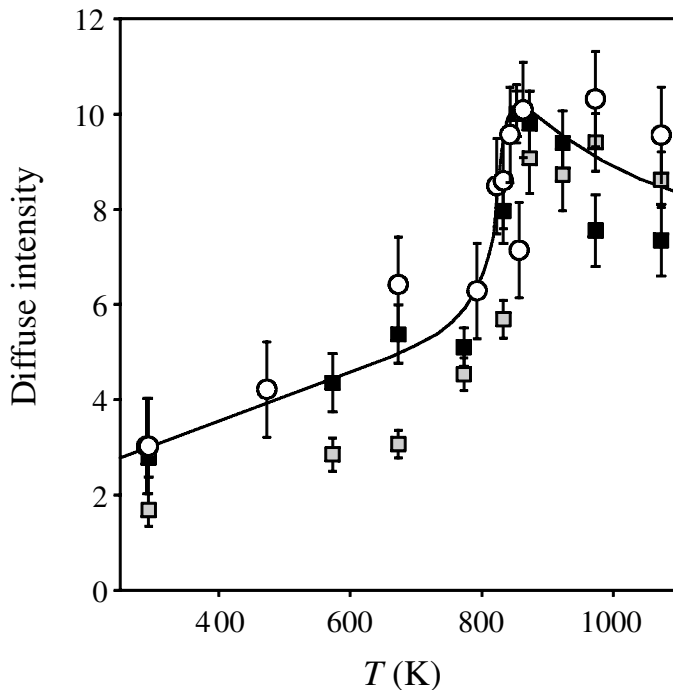
Fig. 15. Temperature dependence of the diffuse intensity in (ζ00) directions. The circles correspond to values from the diffuse scattering obtained from RMC configurations around (4.5,3.5,0), whereas the other data points correspond to the experimental diffuse intensity centred mid-way between (220) and (310) and mid-way between (440) and (530) (grey and black squares, respectively). The line is a guide to the eye through the circles and black squares. All plots have been scaled to give a maximum of 10 at T_c.

crystal diffraction data, albeit with less precision. This conclusively demonstrates that the RMC models do indeed represent a true picture of the structural disorder in quartz. In addition, if we compare the temperature dependence of the intensity of these diffuse features we observe a gradual increase in intensity on heating up to T_c followed by a slight drop above T_c in both the single crystal data and calculated diffuse scattering patterns from the RMC models (see Fig. 15). Within the α-phase the RMC calculated values agree well with the measured (ζ00) branch at higher-Q (black squares in Fig. 15), but less well with the measured (ζ00) branch at lower-Q (grey squares in Fig. 15). This is not necessarily unexpected since different neutron energies (and hence different energy resolutions) are used to measure different portions of the scattering pattern. The higher the neutron energy (which in this case corresponds to higher-Q scattering), the more likely it is to cut higher-energy phonon

branches and hence pick out the diffuse scattering at lower temperatures.

Conclusions

This paper shows that the fine details of the response of the quartz structure to heating through the displacive phase transition can be obtained by utilizing experimental diffraction data and computer modelling. Information on the average structure, the local structure and the dynamic behaviour via the RUM model have all been used to show that, although the symmetry change at the phase transition permeates both the average and the local structural arrangements, it is the increase in thermally-induced structural disorder which dominates the high temperature behaviour in quartz. Various local structural features of this disorder are relatively insensitive to the phase transition although it is argued that overall the disorder in the β-phase is greater than in the α-

phase because this structure allows an increased number of RUMs.

It is particularly encouraging that we have been able to obtain consistency between the results obtained from the various analysis methods. This gives us some confidence to extend this work to investigate in more detail how the RMC models may be used to extract the dynamical processes in quartz more explicitly. This work, which is essentially experiment based, may then be related to molecular dynamics simulations of quartz which are based on established potential functions.

Acknowledgements

References

Arnold, H. (1965) Diffuse Röntgenbeugung und Kooperation bei der α−β-unmandlung von quartz. *Zeits. Kristallogr.*, **121**, 145−57.

Bethke, J., Dolino, G., Eckold, G., Berge, B., Vallade, M., Zeyen, C.M.E., Hahn, T., Arnold, H. and Moussa, F. (1987) Phonon dispersion and mode coupling in high-quartz near the incommensurate phase-transition. *Europhys. Lett.*, **3**, 601.

Bragg, W.L. and Gibbs, R.E. (1925) The structure of α and β quartz. *Proc. Roy. Soc. Lond. A*, **109**, 405−27.

Brown, P.J. and Matthewman, J.C. (1992) *The Cambridge crystallography subroutine library*. Rutherford Appleton Laboratory Report, RAL-92-009.

Carpenter, M.A., Salje, E.K.H., Graeme-Barber, A., Wruck, B., Dove, M.T. and Knight, K.S. (1998) Calibration of excess thermodynamic properties and elastic constant variations due to the α−β phase transition in quartz. *Amer. Mineral.*, **83**, 2−22.

David, W.I.F., Ibberson, R.M. and Matthewman, J.C. (1992) *Profile analysis of neutron powder diffraction data at ISIS*. Rutherford Appleton Laboratory Report, RAL-92-032.

Dove, M.T., Hammonds, K.D., Harris, M.J., Heine, V., Keen, D.A., Pryde, A.K.A., Trachenko, K. and Warren, M.C. (2000*a*) Amorphous silica from the Rigid Unit Mode approach. *Mineral. Mag.*, **64**, 377−88.

Dove, M.T., Pryde, A.K.A. and Keen, D.A. (2000*b*) Phase transitions in tridymite studied using 'Rigid Unit Mode' theory, Reverse Monte Carlo methods and molecular dynamics simulations. *Mineral. Mag.*, **64**, 267−83.

Gibbs, R.E. (1925) The variation with temperature of the intensity of reflection of X-rays from quartz and its bearing on the crystal structure. *Proc. Roy. Soc. Lond. A*, **107**, 561−70.

Grimm, H. and Dorner, B. (1975) On the mechanism of the α−β phase transformation in quartz *J. Phys. Chem. Solids.* **36**, 407−13.

Hahn, T., editor (1996) *International Tables for Crystallography*. Kluwer Academic, Amsterdam, for The International Union of Crystallography.

Hammonds, K.D., Dove, M.T., Giddy, A.P., Heine, V. and Winkler, B. (1996) Rigid unit phonon modes and structural phase transitions in framework silicates. *Amer. Mineral.*, **81**, 1057−79.

Harris, M.J. and Bull, M.J. (1998) *PRISMA single crystal cold neutron spectrometer and diffractometer user manual*, 2nd edition. Rutherford Appleton Laboratory Technical Report, RAL-TR-1998-049.

Harris, M.J., Dove, M.T. and Parker, J.M. (2000) Floppy modes and the Boson peak in crystalline and amorphous silicates: an inelastic neutron scattering study. *Mineral. Mag.*, **64**, 435−40.

Heaney, P.J. (1994) Structure and chemistry of the low-pressure silica polymorphs. Pp. 1−40 in: *Silica: Physical Behavior, Geochemistry, and Materials Applications*. Reviews in Mineralogy, **29**. Mineralogical Society of America, Washington, D.C.

Heaney, P.J. and Veblen, D.R. (1991) Observations of the α−β phase transition in quartz − a review of imaging and diffraction studies and some new results. *Amer. Mineral.*, **76**, 1018−32.

Howe, M.A., McGreevy, R.L. and Howells, W.S. (1989) The analysis of liquid structure data from time-of-flight neutron diffractometry. *J. Phys.: Cond. Matter*, **1**, 3433−51.

Howells, W.S. and Hannon, A.C. (1999) LAD, 1982−1998: the first ISIS diffractometer. *J. Phys.: Cond. Matter*, **11**, 9127−38.

Jay, A.H. (1933) The thermal expansion of quartz by X-ray measurements. *Proc. Roy. Soc.*, **A142**, 237−47.

Liebau, F. (1985) *Structural Chemistry of Silicates: Structure, Bonding and Classification*. Springer-Verlag, Berlin.

Keen, D.A. (1997) Refining disordered structural models using reverse Monte Carlo methods: Application to vitreous silica. *Phase Trans.*, **61**, 109−24.

Keen, D.A. (1998) Reverse Monte Carlko refinement of disordered silica phases. Pp. 101−19 in: *Local Structure from Diffraction* (S.J.L. Billinge and M.F. Thorpe, editors). Plenum Press, New York.

Keen D.A. (2001) A comparison of various commonly used correlation functions for describing total scattering. *J. Appl. Crystallogr.*, **34**, 172−7.

Keen, D.A. and Dove, M.T. (2000) Total scattering

studies of silica polymorphs: similarities in glass and disordered crystalline local structure. *Mineral. Mag.*, **64**, 447—57.

Kihara, K. (1990) An X-ray study of the temperature-dependence of the quartz structure. *Eur. J. Mineral.*, **2**, 63—77.

McGreevy, R.L. and Pusztai, L. (1988) Reverse Monte Carlo simulation: A new technique for the determination of disordered structures. *Molecular Simulations*, **1**, 359—67.

McGreevy, R.L. (1995) RMC — progress, problems and prospects. *Nucl. Inst. Meth. A*, **354**, 1—16.

Pawley, G.S. (1981) Unit cell refinement from powder diffraction scans *J. Appl. Crystallogr.*, **14**, 357—61.

Pusztai, L. and McGreevy, R.L. (1997) MCGR: An inverse method for deriving the pair correlation function from the structure factor. *Physica B*, **234—6**, 357—8.

Toby, B.H. and Egami, T. (1992) Accuracy of pair distribution function-analysis applied to crystalline and noncrystalline materials. *Acta Crystallogr.*, **A48**, 336—46,

Tucker, M.G., Dove, M.T. and Keen, D.A. (2000*a*) Simultaneous analyses of changes in long-range and short-range structural order at the displacive phase transition in quartz. *J. Phys.: Cond. Matter*, **12**, L723—30,

Tucker, M.G., Dove, M.T. and Keen, D.A. (2000*b*) Direct measurement of the thermal expansion of the Si—O bond by neutron total scattering. *J. Phys.: Cond. Matter*, **12**, L425—30.

Tucker, M.G., Dove, M.T. and Keen, D.A. (2001) Application of the Reverse Monte Carlo method to crystalline materials. *J. Appl. Crystallogr.* (in press).

Wright, A.F. and Lehmann, M.S. (1981) The structure of quartz at 25°C and 590°C determined by neutron-diffraction. *J. Sol. State Chem.*, **36**, 371—80.

Young, R.A. (1962) *Mechanism of the phase transition in quartz.* Defence Documentation Center Report, AD276235 Washington 25 DC.